



Design and modeling of a multiscale porous ceramic heat exchanger for high temperature applications with ultrahigh power density

Xiangyu Li^{a,1}, Chad T. Wilson^{a,1}, Lenan Zhang^a, Bikram Bhatia^a, Lin Zhao^a, Army Leroy^a, Olivia Brandt^b, Rodrigo Orta-Guerra^b, Jeffrey P. Youngblood^b, Rodney W. Trice^b, Evelyn N. Wang^{a,*}

^a Department of Mechanical Engineering, Massachusetts Institute of Technology, USA

^b School of Materials Engineering, Purdue University, USA

ARTICLE INFO

Article history:

Received 7 November 2021

Revised 27 March 2022

Accepted 2 May 2022

Keywords:

High temperature heat exchanger
Finite element numerical simulation
Compact heat exchanger
Co-extrusion
Porous media approach

ABSTRACT

The efficiency of a heat engine can be significantly improved by operating in a high-temperature and high-pressure environment, which is crucial for a wide range of applications such as hybrid and electric aviation as well as power generation. However, such extreme operating conditions pose severe challenges to the heat exchanger design. Although recently developed superalloys and ceramics can survive high-temperature and high-pressure loads, using these materials in a traditional heat exchanger design requires high cost and yields low power density. In this work, we propose an ultrahigh power density ceramic heat exchanger for high-temperature applications enabled by a multiscale porous design. By optimizing the design of centimeter-scale macrochannels and microchannels, significant improvement to both heat transfer and structural strength is predicted, with a negligible pressure drop penalty ($< 1\%$). Based on finite element simulations, an optimized heat exchanger core design is expected to achieve power densities of 717 MW/m^3 and 300 kW/kg , which indicates more than $2.5\times$ enhancement in thermal performance compared to printed-circuit heat exchanger design. Furthermore, the heat exchanger design features low material costs and scalable fabrication, enabling highly customizable applications in aerospace and terrestrial power generation.

© 2022 Elsevier Ltd. All rights reserved.

1. Introduction

Ninety percent of global energy is related to the manipulation of heat [1], which is the reason centuries of efforts have been dedicated to enhancing the efficiency of heat engines. Operating thermal systems in high-temperature and high-pressure conditions predicts a higher overall thermodynamic efficiency [2,3], promising significant impact on the terrestrial power generation systems [4–6], and hybrid and electric aviation [7–9]. To enable these high-temperature and high-pressure applications, the development of a high-performance heat exchanger plays a key role [3,10]. Despite significant advances in materials such as superalloys [11,12] and ceramics [13,14], there lacks a generic heat exchanger design to further enhance the heat exchanger performance with low-cost fabrication. Plate-fin and plate-and-frame heat exchangers use thin sheets to separate two working fluids, thus are often challenging due to the high operating temperatures and pressure difference.

The conventional shell-and-tube heat exchanger design is capable of higher temperatures and pressures, but suffers from low-power density due to low surface area to volume ratio. It also requires a large amount of material and hence leads to high cost for high-temperature applications [10].

As additive manufacturing enables a much larger design space, manifold-microchannel heat exchangers leverage the benefits of microchannels, combining high heat transfer coefficient with short flow length to achieve up to 10 kW/kg power density at 50% effectiveness and a surface area per volume ratio of $1000\text{--}2000 \text{ m}^2/\text{m}^3$ [15–18]. Multi-furcating and advanced fin-and-tube heat exchangers have reached similar performance with complicated geometries that are only possible with additive manufacturing [19,20]. With channels close to 1 mm, a conventional shell-and-tube heat exchanger design can reach the surface area to volume ratio of $2000 \text{ m}^2/\text{m}^3$ [11]. Using photo-chemical etching, printed-circuit heat exchangers (PCHE) have shown promise for extreme conditions, with semi-circular straight channel widths around 2 mm [21] and volumetric power density up to 4 MW/m^3 with Ni-based superalloys, or 9 MW/m^3 based on Zr/W [14]. Other channel topologies to enhance thermal transport have also been studied

* Corresponding author.

E-mail address: enwang@mit.edu (E.N. Wang).

¹ These authors contributed equally to this work.

Nomenclature

k_{eff}	effective thermal conductivity W/m K
k_{SiC}	thermal conductivity of SiC W/m K
t_w	thickness of SiC between microchannels m
D	internal side length of square microchannel m
t_M	thickness of a macrochannel wall m
D_M	internal side length of square macrochannel m
L	length of microchannel m
u	vector flow field m/s
P	pressure of fluid N/m ²
T	temperature K
C_p	specific heat capacity at constant pressure J/kg K
E	Young's modulus for SiC N/m ²
S	second Piola-Kirchhoff stress tensor N/m ²
E	Green-Lagrange strain tensor
I	identity matrix
F	deformation gradient
C	right Cauchy-Green deformation tensor
A	area m ²

Greek symbols

φ	porosity of the microchannel array
σ_{UTS}	ultimate tensile strength N/m ²
ρ	density kg/m ³
σ	Cauchy stress tensor N/m ²

Subscripts and abbreviations

<i>cold</i>	cold side of the heat exchanger
<i>hot</i>	hot side of the heat exchanger
<i>SiC</i>	silicon carbide
<i>avg</i>	average
<i>hi</i>	high
<i>lo</i>	low

to enhance power density while maintaining low pressure drop, such as airfoil fins [22], zigzag [23] and square channels [24]. However, photo-chemical etching on superalloys is an expensive and slow process, and the diffusion bonding method relies on a high-pressure treatment for an extended period of time, both posing challenges in scalability and low-cost fabrication [25].

Therefore, the challenge still exists to develop scalable, low cost, compact high temperature heat exchanger designs in combination with suitable manufacturing techniques. Here, we present a multiscale porous ceramic heat exchanger design, enabling the simultaneous enhancement of thermofluidic transport and mechanical strength. Our design of the heat exchanger core leverages a scalable ceramic co-extrusion process [26–28] to create centimeter-scale macrochannels which consist of straight microchannels. The microchannels increase the surface area to enable significant heat transfer enhancement, and the scaffold structure formed by the microchannel array reinforces the overall mechanical strength to overcome the high-pressure loadings of operation. By utilizing straight microchannels rather than random porous media, the working fluids experience a much smaller pressure drop penalty. To model and optimize the co-extruded heat exchanger core, we developed a hierarchical model including thermofluidic simulation and structural analysis. With air and sCO₂ as working fluids in hybrid and electric aviation applications, we show power densities of 717 MW/m³ and 300 kW/kg with 50% thermal effectiveness, more than an order of magnitude higher than conventional shell-and-tube heat exchanger designs [10]. With molten salt and sCO₂ as working fluids in terrestrial power generation, the heat exchanger based on our design can achieve power densities of 9.71 MW/m³ and 4.05 kW/kg with 95% effectiveness, which is 2.5× thermal per-

formance compared to printed circuit heat exchangers with similar materials [2,11,14].

2. Methods

Fig. 1 shows the concept of the multiscale porous ceramic heat exchanger design, which consists of counter-flow centimeter-scale square macrochannels (white dashed box in Fig. 1(a)) and microchannels (small squares in the white dashed box in Fig. 1(a)). The cold (purple regions in Fig. 1(a)) and hot (red regions in Fig. 1(a)) working fluids flow along opposite directions, denoted by the purple and red arrows in Fig. 1(a), in a checkerboard macrochannel pattern. Fig. 1(b) shows a schematic of a single macrochannel comprising the microchannel array, which can be fabricated by an established scalable co-extrusion process, where centimeter channels can be reduced to the order of 100 μm after three co-extrusion processes [26–28]. The straight microchannels provide high permeability, leading to low pressure drop. Owing to the lower thermal resistance of the thin solid walls, the microchannel array significantly enhances the heat spread in the macrochannel (Fig. 1(b)), resulting in better heat transfer than the conventional macrochannel (Fig. 1(c)). Additionally, the scaffold structure formed by microchannel walls (Fig. 1(d)) enhances the overall mechanical strength, resulting in less mechanical deformation under high-pressure operation (dashed lines in Fig. 1(d, e)). To quantitatively optimize the thermal and mechanical performance of the proposed design, we develop thermofluidic and mechanical models, which will be described in the following sections.

In this work, SiC was adopted as the preferred solid material due to its low cost, high thermal conductivity, high melting point and stable mechanical strength at high temperatures. More importantly, the co-extrusion fabrication of ceramics similar to SiC has been well-established [26–28]. The material properties of 3C-SiC are included in Appendix A. We chose the working fluids as air at 1285 °C and 80 bar and supercritical CO₂ at 300 °C and 250 bar as an example based on potential aviation applications [6–8]. Both flows maintain identical flow rates of 0.004 kg/s per macrochannel to achieve similar heat capacity flows (heat capacity ratio Cr = 1) for high power density and heat exchanger effectiveness. Additionally, the selected flow rates enable laminar flows in the microchannels for low pressure drops.

2.1. Thermofluidic modeling

Fig. 2 shows a hierarchical framework to model the thermofluidic transport in the proposed multiscale porous heat exchanger. We started with modeling fluidic flow in an individual microchannel to study the pressure drops and flow velocity profiles (Fig. 2(a)). Then the velocity profiles were imported to the microchannel network to quantify the enhanced thermal transport with an array of microchannels (Fig. 2(b)). However, to simulate the entire macrochannel heat exchanger core, heat transfer of ≈ 2500 microchannels needs to be solved simultaneously, which is computationally prohibitive. To provide an efficient model for thermal performance prediction and optimization, an effective medium approach was adopted, which approximates each microchannel network as a homogeneous medium. Therefore, instead of simulating the detailed microstructures within each macrochannel, they are replaced by the effective medium with a simple geometry, which significantly reduces the computational cost. In Fig. 2(c), the top 25 and bottom 25 microchannels were modeled as two homogeneous media, with an effective microporosity ϕ and an effective thermal conductivity of the homogeneous media k_{eff} . We utilized constant thermophysical properties and fully developed fluidic flows to validate the effective thermal conductivity, and how it is related to the microporosity of the microchannel network and

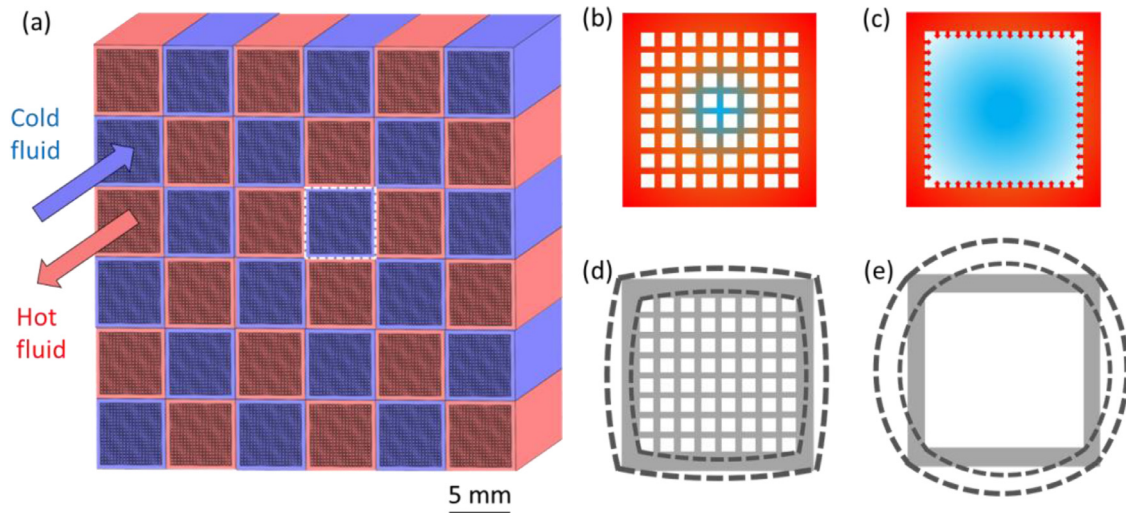


Fig. 1. Schematics of the multiscale porous ceramic heat exchanger design. (a) The counterflow heat exchanger consists of macrochannels (white dashed box) in a checkerboard pattern. (b) A single macrochannel comprises the microchannel array, enhancing the heat spread in the macrochannel due to lower thermal resistance of the thin solid walls, compared to the conventional macrochannel in (c). (d) The microchannel walls also reinforce the mechanical strength. (e) Comparably without microchannels, the macrochannel walls experience significantly higher stress and deformation. The dashed lines in (d,e) represent the magnified deformation of the macrochannel walls under the high-pressure loadings.

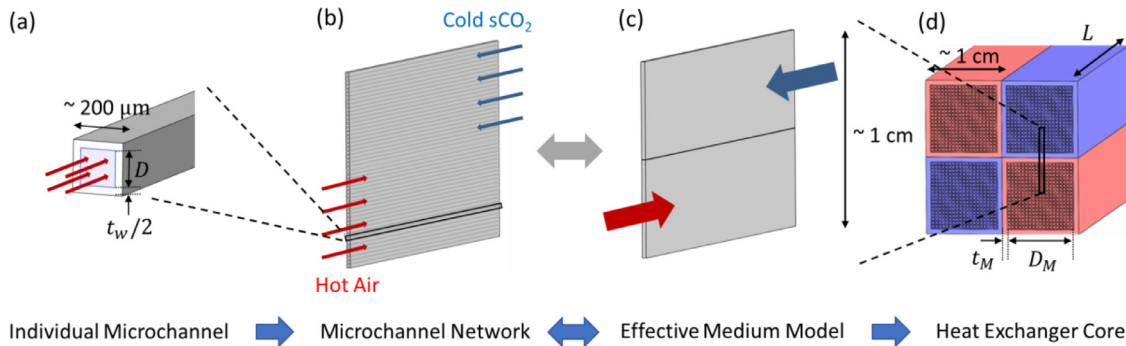


Fig. 2. Schematic of the hierarchical framework for thermofluidic modeling of the heat exchanger core. (a) The model of individual microchannels provides pressure drops and velocity profiles to study the heat transfer in (b) the microchannel network. (c) An effective medium model is developed to interface the microchannel network with the macrochannel heat exchanger core and hence reduces the computational cost. (d) Results given by the effective medium model are used as inputs of the macrochannel model to predict the thermal performance of the heat exchanger core.

solid thermal conductivity. We swept a wide range of solid thermal conductivities to demonstrate that the effective medium model was validated across the operating temperatures by comparing to the temperature response of the detailed microchannel network. Lastly, results given by the effective medium model were used as inputs of the macrochannel model to predict the thermal performance of the heat exchanger core (Fig. 2(d)). The macrochannel cores were modeled as the effective media, while the macrochannel walls were treated as bulk SiC. To predict the heat exchanger performance, realistic thermophysical properties with temperature dependency were applied to both the macrochannel cores and SiC walls. Periodic conditions were applied at the boundary planes parallel to the flow directions. The entirety of this hierarchical framework was implemented in COMSOL Multiphysics.

The thermofluidic numerical simulations were conducted using finite element method in COMSOL Multiphysics v5.5. Details of this method are included in Appendix B. The hierarchical model consists of COMSOL simulations for an individual microchannel, microchannel network, effective medium model, and the overall heat exchanger core optimization. Temperature-dependent material properties of SiC, air and sCO₂ were applied based on literature for the overall heat exchanger core optimization, with SiC properties listed in Appendix A. All simulations were steady-state studies.

The simulation for individual microchannels includes the computational fluid dynamics (CFD) module. The flow field is described by mass conservation (Eq. (1)) and Navier-Stokes (Eq. (2)) equations for the steady-state study,

$$\frac{1}{\rho} \frac{D\rho}{Dt} + \nabla \cdot \mathbf{u} = 0 \tag{1}$$

$$\rho \frac{\partial \mathbf{u}}{\partial t} + \rho(\mathbf{u} \cdot \nabla)\mathbf{u} = -\nabla p + \nabla \cdot [\mu(\nabla \mathbf{u} + (\nabla \mathbf{u})^T)] \tag{2}$$

where \mathbf{u} , and p are the vector flow field and pressure, respectively. A mesh containing boundary layers near the wall is generated for the microchannel fluidic model. Boundary layer properties are defined as 8 layers with a stretching factor of 1.2, automatic thickness prescribed for the first layer, and a thickness adjustment factor of 5, all recommended parameters set as default for laminar flow in COMSOL [29]. The inlet flow was defined with a uniform velocity, designed inlet temperature, and the boundary condition of the fluidic flow was set as non-slip condition.

For the microchannel network and the effective medium model, constant properties and fully developed flows were assumed in the simulation. In the microchannel network model, 50 microchannels were aligned, and both hot air and sCO₂ flow through 25 microchannels in opposite directions. The thermal transport of the

working fluids is described by Eq. (3),

$$-\nabla \cdot (\kappa \nabla T) + \rho C_p \mathbf{u} \cdot \nabla T = 0 \quad (3)$$

where κ , ρ , C_p and T are the thermal conductivity, density, heat capacity and temperature, respectively. To reduce the computational cost, the velocity profiles of the fully developed flow were assigned from the model for individual microchannels. The effective heat capacity, flow rate, and density were averaged to maintain mass and energy balance. The outlet temperatures were averaged based on the heat capacity flows. Effective thermal conductivity k_{eff} was evaluated based on the microchannel geometry,

$$k_{eff} \approx \frac{t_w(D + t_w)}{t_w^2 + D^2 + t_w D} k_{SiC} \quad (4)$$

where D is the microchannel pore size, t_w is the wall thickness between adjacent microchannels, and k_{SiC} is the bulk SiC thermal conductivity.

2.2. Mechanical stress modeling

To ensure the sufficient mechanical strength of the proposed design for the high-temperature and high-pressure operation, we developed a structural model to identify the locations where stress profiles in the SiC material are at a maximum and optimize the heat exchanger core geometry to avoid failure due to fast-fracture of the brittle SiC.

A porous medium approximation of microchannel arrays, similar to the approach for thermal modeling, was adopted to efficiently evaluate the mechanical response of SiC macrochannels under static pressure loading conditions. Each macrochannel consists of a 5 mm by 5 mm porous media region enshrouded by walls of varying widths. The 1st principal stress [30] is the maximum tensile stress in our model, since SiC has an ultimate strength several orders of magnitude less in tension than compression [31], and thus is most likely to experience failure due to fast-fracture when local 1st principal stress values exceed its ultimate tensile strength limit ($\sigma_{UTS} = 500$ MPa) [32]. We varied macrochannel wall thickness and microporosity ϕ to identify geometric configurations that significantly impact stress fields in the SiC. Material properties that remain constant in this porous medium approximation are taken from literature and listed in Table A1. Young's modulus for the porous media E_{pore} is estimated as [31]

$$E_{pore} = E_{SiC} (1 - \phi) \left(1 - \frac{\phi}{0.684} \right) \quad (5)$$

where ϕ is the microporosity of the medium, and E_{SiC} is the Young's modulus for bulk SiC. The density of the porous medium ρ_{porous} is also dependent on microporosity and is defined as $(1 - \phi)\rho_{SiC}$. Finite element analysis of the heat exchanger core was performed using a total Lagrangian formulation for finite deformations in COMSOL v5.5. Eq. (6) is the governing equation for the 2D elastic model of SiC,

$$\nabla \cdot \mathbf{S} + \mathbf{F}_v = 0 \quad (6)$$

where \mathbf{S} is the second Piola-Kirchhoff stress tensor [33] and \mathbf{F}_v denotes body force terms that are absent in this application.

We systematically solved for the displacements that satisfy this governing equation by implementing a finite deformation, isotropic linear elastic framework. First, this finite strain model used Eq. (7) to relate deformation to the Green-Lagrange strain tensor \mathbf{E} ,

$$\mathbf{E} = \frac{1}{2} (\mathbf{F}^T \mathbf{F} - \mathbf{I}) = \frac{1}{2} (\mathbf{C} - \mathbf{I}) \quad (7)$$

where \mathbf{I} is the identity matrix, \mathbf{F} is the deformation gradient and \mathbf{C} is the right Cauchy-Green deformation tensor [33]. Then, for a

linear elastic material, Hooke's Law related the elastic strain tensor to the Second Piola-Kirchhoff stress tensor using Eq. (8),

$$\mathbf{S}_{ij} = 3K \left(\frac{1}{3} E_{kk} \delta_{ij} \right) + 2G \left(E_{ij} - \frac{1}{3} E_{kk} \delta_{ij} \right) \quad (8)$$

where K is the bulk modulus and G is the shear modulus of the material, and δ is the Kronecker delta function. Furthermore, \mathbf{S} is related to the Cauchy stress tensor $\boldsymbol{\sigma}$ by Eq. (9),

$$\boldsymbol{\sigma} = \mathbf{J}^{-1} \mathbf{F} \mathbf{S} \mathbf{F}^T \quad (9)$$

where $\mathbf{J} = \det(\mathbf{F})$. Principal stress values are defined as the eigenvalues of the Cauchy stress tensor $\boldsymbol{\sigma}$ and are the primary output of the numerical model used in this analysis.

Since the pressure loading difference within both hot and cold porous cores, 80 bar (P_{lo}) and 250 bar (P_{hi}), respectively, occurs uniformly in the macrochannel, we applied a traction boundary condition on the interior walls of each macrochannel equivalent to working fluid operating pressures. Symmetric boundary conditions were applied to the model's external edges to produce a periodic solution that can be extrapolated for heat exchangers with differing macrochannel array sizes. All other boundaries were modeled with free boundary conditions. Fig. 3 depicts the finite element mesh, associated boundary conditions as well as the macrochannel fillet area where maximum 1st principal stress values are averaged. Filleted corners on the length scale of expected grain size ($\sim 5 \mu\text{m}$) are expected following the sintering of SiC and allow for average maximum stress values to be repeatably obtained [34]. After establishing the finite element framework, mesh refinements reported in Appendix B were performed to an error tolerance of 0.001 to ensure repeatability of the simulation.

3. Results and discussion

Fig. 4 shows the fully developed velocity profiles (Fig. 4(a, b)) and pressure drops (Fig. 4(c, d)) in the air and sCO₂ microchannels. The microscale feature leads to a laminar flow regime with low Reynolds number (~ 500 to ~ 1800), which helps reduce the pressure drop. To highlight the significance of the straight microchannel design in optimizing the fluidic performance, we compared the pressure drop along a straight microchannel with that along a random porous foam, which is commonly used for heat transfer and mechanical strength enhancement. Fig. 4(c, d) shows the pressure drop of air (Fig. 4(c)) and sCO₂ (Fig. 4(d)) flows under different flow velocities, Reynolds numbers and microchannel sizes. The dashed lines represent the pressure drop of a random porous aluminum foam [35] under the same pore sizes and flow rates as the microchannels, predicted by the Darcy's Law. For both cases, pressure drop increases with smaller channel sizes and higher flow rates. The effects of entrance length and thermal gradient on the pressure drop are discussed in Appendix C, including the validation for air and sCO₂ fluids.

With the velocity profile predicted by the single microchannel simulation as an input, we are able to simulate the heat transfer in a microchannel network. The microchannel network consists of 50 microchannels aligned in a one-dimensional array (Fig. 2(b)). Hot air (1285 °C, 80 bar) flows through the top 25 microchannels while cold sCO₂ (300 °C, 250 bar) flows through the bottom 25 microchannels in the opposite directions (Fig. 2(b)). Boundary conditions for the microchannel network simulation can be seen in the Methods section. Fig. 5(a) shows the temperature profile of the microchannel network.

Comparison of the effective medium model (Fig. 5(b)) to the microchannel network simulation (Fig. 5(a)) shows good agreement in temperature profiles. Fig. 5(c) shows the temperature profiles along three representative directions (labeled as 1, 2, and 3) parallel to the flow direction, whereas Fig. 5(d) shows the temperature profiles along three perpendicular directions (labeled as

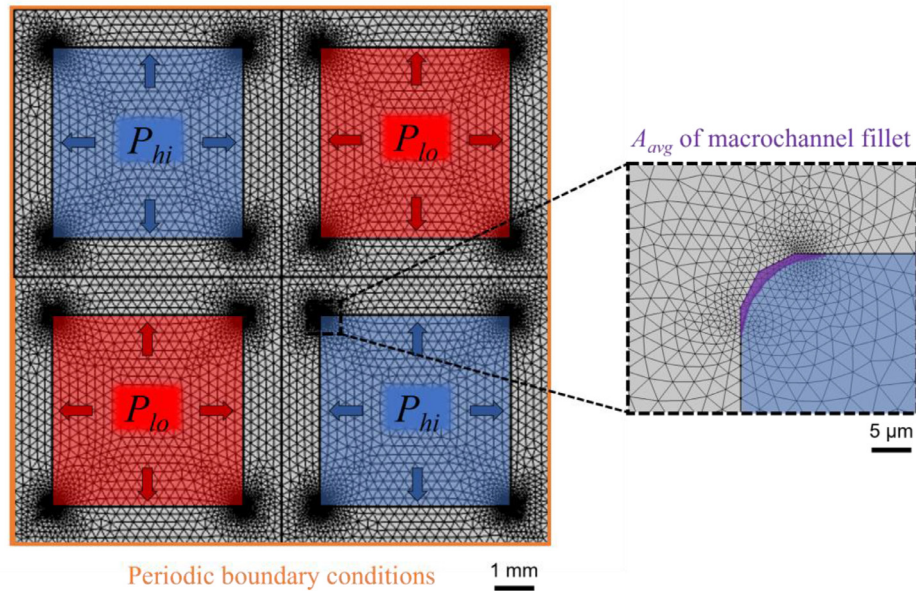


Fig. 3. Finite element mesh, boundary and loading conditions for structural mechanics COMSOL simulation. Fluid pressure was applied as a static, uniformly distributed load on macrochannel walls, while a periodic boundary condition was prescribed on the exterior boundary of alternating channels to emulate a scalable checker-board heat exchanger core.

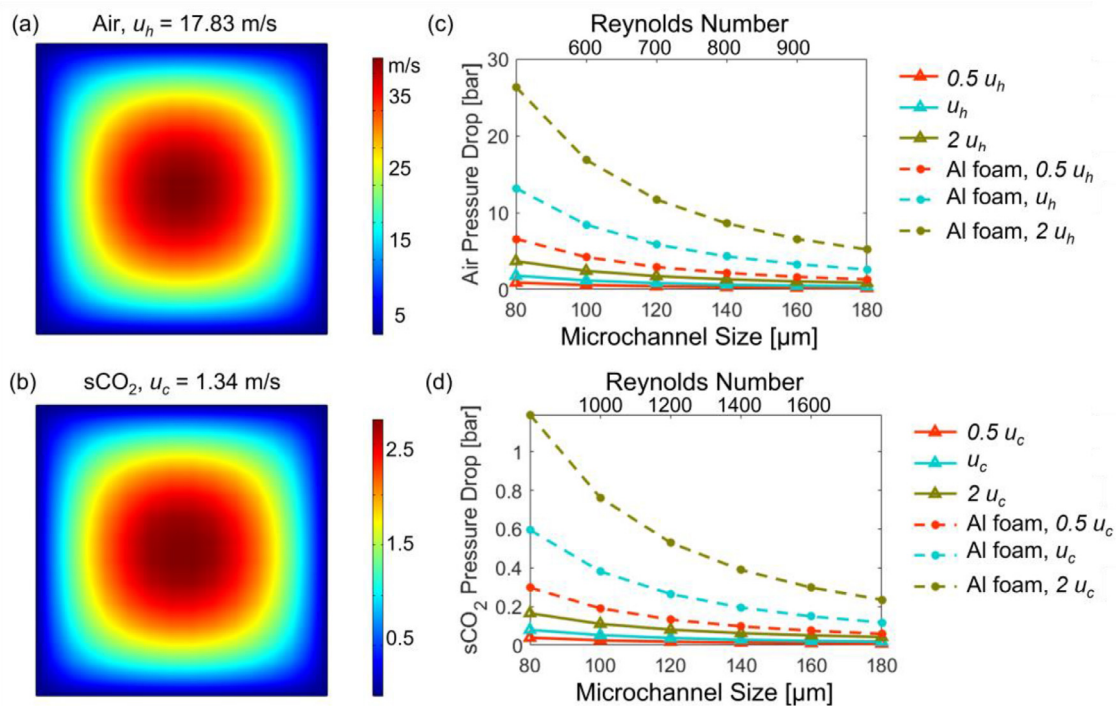


Fig. 4. Fluidic simulation results of air and sCO₂ flows through microchannels under different microchannel sizes and velocities. (a, b) Fully developed velocity profiles of the air and sCO₂ flows in microchannels with u_h and u_c as the average flow rates, respectively. (c, d) Pressure drops of the air and sCO₂ flows under different flow velocities, Reynolds numbers and microchannel sizes, respectively. The dashed lines represent the pressure drop with random porous media based on the Darcy’s Law with the same pore sizes and flow rates as the microchannels. Note that the Reynolds numbers for the air flow and sCO₂ flow are determined by u_h and u_c , respectively.

1’, 2’, and 3’). Quantitative agreement between the microchannel network simulation and the effective medium model was demonstrated. We further validated the broad applicability of the effective medium model under a wide range of microporosities ϕ from 0.3 to 0.7 and solid thermal conductivity k_{SiC} of 10–300 W/mK. Fig. 5(e) shows the temperature T_1 at the air flow outlet (blue spot in Fig. 5(a)) as a function of the solid thermal conductivity under different microporosities. The temperature response was pre-

cisely captured by the effective medium model. In addition, we directly extracted the effective thermal conductivity from the microchannel network simulation and compared it with the analytical expression in Eq. (4). As shown in Fig. 5(f), Eq. (4) provides a highly accurate approximation for the effective thermal conductivity within the full range of solid thermal conductivity up to 300 W/mK, which covers the SiC thermal conductivity in the operation condition (573–1558 K). Although only a one-dimensional

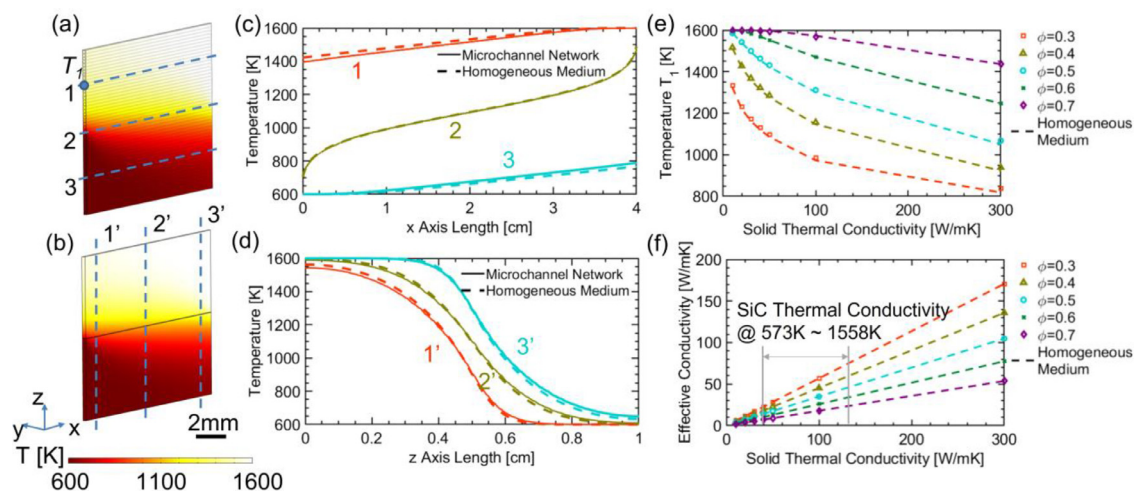


Fig. 5. Simulation results of the microchannel network using COMSOL finite element simulations, compared to the effective medium model. (a, b) Temperature profiles from the microchannel network and the effective medium model, demonstrating qualitative agreement. (c, d) Temperature profiles along three representative directions (labeled as 1, 2, and 3) parallel to the flow direction, and three perpendicular directions (labeled as 1', 2', and 3'). Solid lines represent the simulation results from the microchannel network, and dashed lines represent the effective medium model using homogeneous media. (e) Temperature T_1 as a function of different solid thermal conductivities and microporosities. (f) The effective thermal conductivity is extracted from the microchannel network simulation and compared with the analytical expression in Eq. (4).

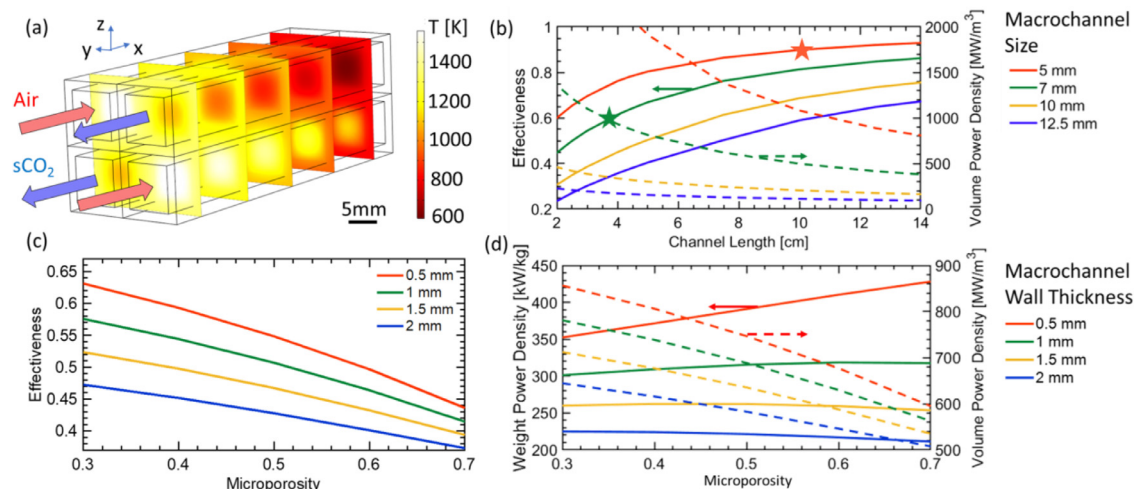


Fig. 6. Heat exchanger core optimization for thermal performance. (a) The microchannel network and flows are modeled as homogeneous media in the macrochannels with periodic boundary conditions. (b) Effectiveness of the heat exchanger as a function of channel length and macrochannel size, which includes the microchannel array as well as the macrochannel walls. Green star represents a design to achieve an effectiveness of 0.5, while red star for an effectiveness of 0.9. Microporosity (c) and macrochannel wall thickness (d) are optimized for heat exchanger effectiveness, volume and weight power densities while maintaining the same macrochannel size.

microchannel array was investigated here, the effective medium approach is applicable for a two-dimension array of a microchannel network as the macrochannel core. The radiation effect is neglected due to the much lower radiative heat transfer compared to convective and conductive heat transfer. The heat exchanger core system is insulated from the ambient during operation. More information is provided in Appendix D.

Results for a unit cell of the heat exchanger core comprising four macrochannels in counterflow configuration is shown in Fig. 6(a). Identical mass flow rates were assumed in each macrochannel. The temperature profile of this unit cell was simulated (Fig. 6(a)), from which the key metrics of thermal performance including the effectiveness and power densities can be evaluated. We performed a parametric study to elucidate the design tradeoff related to the channel length, macrochannel size, macrochannel wall thickness and microporosity. Fig. 6(b) shows the design tradeoff between the effectiveness and volume power density due to the change of channel length. The increase of channel length leads to the increase of heat exchanger effectiveness

while reducing the volume power density due to the increase of heat exchanger total volume. Another perspective is that the length of the channels increases the NTU, which enhances the effectiveness. More information is provided in Appendix E. One of the key design parameters is the macrochannel size. Smaller macrochannels are preferred to achieve much higher effectiveness and higher volumetric power density with the same channel length, because large macrochannels increase the overall conduction resistance within the effective media in the macrochannel core. This provides a possible approach to enhance effectiveness without posing longer channels or high pressure drop, although the macrochannel size can be limited by possible fabrication constraints. We identified two design examples related to an effectiveness of 0.5 (green star) and 0.9 (red star). Note that when pursuing high volume power density ($> 500 \text{ MW/m}^3$) applications, this tradeoff becomes particularly significant, as shown in the regime with the channel length smaller than 9 cm and macrochannel size smaller than 7 mm. Fig. 6(c, d) shows that reducing microporosity can significantly enhance both the effectiveness and volume power

Table 1
Comparison of surface area to volume ratio among different heat exchanger designs.

	A_{heat}/V [m^2/m^3]	T_{max} [$^{\circ}\text{C}$]	P_{max} [bar]	Refs.
Shell-and-tube heat exchanger	50–100	1100	1000	[36]
Plate-and-frame heat exchanger	120–660	815	200	[36]
Plate-fin heat exchanger	800–1500	800	200	[11,37]
Printed circuit heat exchanger	200–2500	980	900	[11,38]
Multiscale porous heat exchanger	7143	1285	250	This work

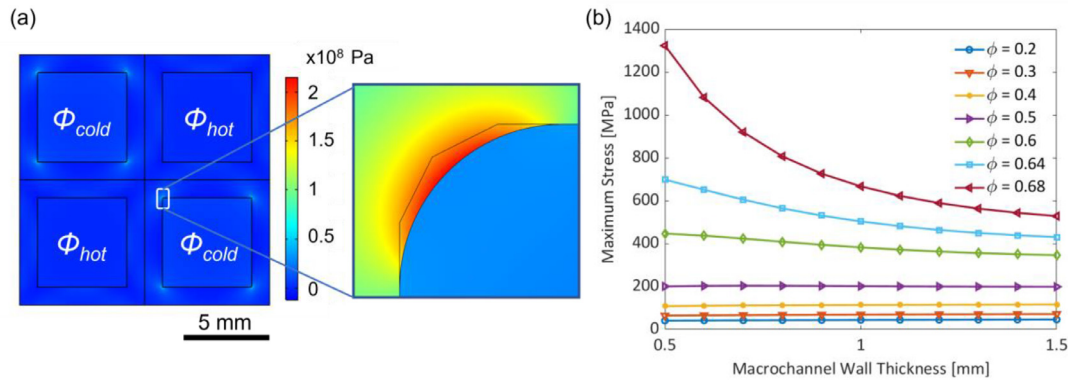


Fig. 7. Structural analysis of heat exchanger core. (a) Four macrochannels were simulated with periodic conditions. The zoomed-in figure shows macrochannels with 1 mm wall thickness. Effective Young's modulus for the porous media was applied in the microchannel network for varying microporosities (microporosity $\phi = \phi_{\text{hot}} = \phi_{\text{cold}}$). (b) Maximum stress experienced by the heat exchanger is highly dependent on the microporosity of the microchannel network rather than the wall thickness, especially when microporosity reaches 50%.

density due to the increase of effective thermal conductivity (Eq. (4)), inducing a slight decrease of the weight power density due to the increase of total mass with microporosity (Fig. 6(d)). For example, there is an approximately 20% increase of both the effectiveness and volume power density when reducing the microporosity from 0.7 to 0.5. However, note that the effectiveness enhancement by increasing channel length and decreasing microporosity also leads to higher pressure drops, which can be a limiting factor for working fluids with higher viscosities or larger flow rates. More information of pressure drop in the heat exchanger core is provided in Appendix C. On the other hand, it is always desirable to pursue thinner macrochannel walls to enhance effectiveness, volume, and weight power densities simultaneously. For example, there are approximately 10%, 10%, and 25% increases of effectiveness, volume, and weight power densities, respectively, when reducing the macrochannel wall thickness from 1 to 0.5 mm with a microporosity of 0.5. However, note that approaching the minimal macrochannel wall thickness is fundamentally limited by the fabrication processes. Overall, to pursue high volume power density over $500 \text{ MW}/\text{m}^3$ and effectiveness larger than 0.5, a reasonable design space should target the channel shorter than 14 cm, macrochannel size smaller than 10 mm, microporosity lower than 0.6, and macrochannel wall thinner than 2 mm. Despite the short channel length and high thermal gradient, the solid conductive heat transfer in the axis direction can be neglected. More information on this conclusion is shown in Appendix E.

Mechanical modeling results of the heat exchanger core with varying macrochannel wall thicknesses and microporosities are shown in Fig. 7. The maximum tensile stress occurs at the filleted corners of the macrochannels (Fig. 7(a)) and is reported in Fig. 7(b) as a function of both wall thickness and microporosity. Overall, the maximum tensile stress is dominated by the microporosity rather than the wall thickness, when microporosity reaches 50%. The porous structure formed by the microchannel network mitigates the stringent structural requirement by reducing the dependency of wall thickness on the stress profile, thus significantly reducing the volume, and enhancing the power densities, of the

heat exchanger. Predicted maximum 1st principal stress values of approximately 200 MPa provide a safety factor of 2.5 against SiC fast fracture for a heat exchanger with microporosity of 50%, macrochannel wall thickness of 1 mm, and macrochannel pore size of 5 mm, which falls into the proposed design space based on the thermofluidic analysis. More information on thermal stress is provided in Appendix F.

Enabled by the microchannel network, the proposed heat exchanger can achieve a surface area to volume ratio of $7143 \text{ m}^2/\text{m}^3$, as shown in Table 1 [10]. This enables high power densities ($717 \text{ MW}/\text{m}^3$, $300 \text{ kW}/\text{kg}$) of the proposed multiscale porous ceramic heat exchanger with the design parameters determined from the thermofluidic and mechanical strength models, as summarized in Table 2, which indicates more than one order of magnitude enhancement compared to convective heat exchanger designs. It is also possible to pursue even higher power densities if the limits due to the fabrication process and pressure drop can be further relaxed. According to the existing co-extrusion process [26–28], a feature size of $60 \mu\text{m}$ was chosen as the microchannel wall thickness. The microchannel core size was adopted as $140 \mu\text{m}$ microchannels with 50% microporosities, which enhances thermal performance, satisfies the requirement for structural strength, and provides a low pressure drop below 1%. The effect of possible fabrication defects is discussed in Appendix G. Future work includes the design of headers for the proposed heat exchanger core, with one possible header design included in Appendix H that promises uniform mass distribution and minimal pressure drop.

Furthermore, guided by the hierarchical thermofluidic model, the proposed heat exchanger can be customized for other applications including terrestrial power generation, such as nuclear power plants and concentrated solar power systems. Due to the high viscosity of the molten salt and high effectiveness requirement in these applications, larger microchannels are assigned to address the pressure drop challenge. Table 2 includes a heat exchanger design with a thermal duty of $17.5 \text{ MW}_{\text{th}}$, 95% effectiveness, power densities of $9.71 \text{ MW}/\text{m}^3$ and $4.05 \text{ kW}/\text{kg}$, more than $2.5\times$ thermal performance compared to printed-circuit heat exchangers with

Table 2
Summary of the heat exchanger designs for aviation and concentration solar power systems.

Parameter	Aviation	Concentrated solar power
Microchannel size	140 μm (air, sCO ₂)	140 μm (sCO ₂); 0.7 mm (molten salt)
Microchannel wall	60 μm (air, sCO ₂)	60 μm (sCO ₂); 0.3 mm (molten salt)
Macrochannel core	5 mm	5 mm
Macrochannel wall	1 mm	1 mm
Channel length	4 cm	25 cm
Effectiveness	50%	95%
Volume power density	717 MW/m ³	9.71 MW/m ³
Mass power density	300 kW/kg	4.05 kW/kg

similar materials [2,11,14]. More detailed information can be found in Appendix I.

4. Conclusions

In this work, a multiscale porous ceramic heat exchanger design was proposed, which offers a highly modular and customizable approach with high performance for a wide variety of high-temperature high-pressure applications based on numerical simulations of a hierarchical thermofluidic model and stress model with COMSOL Multiphysics. An optimized SiC heat exchanger with air and sCO₂ working fluids can achieve a surface area to volume ratio of 7143 m²/m³, 2.8 \times enhancement compared to state-of-the-art heat exchangers. Our simulation predicts a power density of 717 MW/m³, 300 kW/kg with 50% thermal effectiveness, while maintaining a pressure drop lower than 1% and a safety factor against failure of 2.5. Furthermore, our proposed heat exchanger can also be customized for other applications including terrestrial power generation plants. With working fluids of molten salt and sCO₂, an optimized design can achieve a thermal duty of 17.5 MW_{th}, 95% effectiveness, power densities of 9.71 MW/m³ and 4.05 kW/kg. Overall, our proposed heat exchanger promises more than 2.5 \times thermal performance compared to printed-circuit heat exchangers utilizing similar materials, while providing the benefits of low cost, scalable fabrication, low pressure drops and high structural strength. To better understand the fundamental thermal performance limit of this proposed design, a thorough thermodynamic analysis is useful in the future for both the heat exchanger component and its relationship to the proposed sCO₂ Brayton cycle.

Author statement

The authors thank Dr. Gregory Natsui and Dr. Kristen Brosnan from General Electric for valuable discussions. The authors thank Eric Stewart for his guidance on the fundamentals of mechanical modeling. This research was supported by Advanced Research Projects Agency-Energy (Award No. DE-AR0001130).

Declaration of Competing Interest

A provisional patent application (U.S. Patent: 63/166,973) was filed based on this work on March 27, 2021.

CRedit authorship contribution statement

Xiangyu Li: Conceptualization, Methodology, Investigation, Writing – original draft, Writing – review & editing. **Chad T. Wilson:** Methodology, Investigation, Writing – original draft, Writing – review & editing. **Lenan Zhang:** Conceptualization, Methodology, Investigation, Writing – review & editing. **Bikram Bhatia:** Conceptualization, Writing – review & editing, Funding acquisition. **Lin**

Zhao: Methodology, Writing – review & editing. **Arny Leroy:** Conceptualization, Writing – review & editing. **Olivia Brandt:** Methodology. **Rodrigo Orta-Guerra:** Methodology. **Jeffrey P. Youngblood:** Conceptualization, Writing – review & editing. **Rodney W. Trice:** Conceptualization, Writing – review & editing. **Evelyn N. Wang:** Conceptualization, Writing – review & editing, Funding acquisition, Resources, Supervision.

Acknowledgments

The authors thank Dr. Gregory Natsui and Dr. Kristen Brosnan from General Electric for valuable discussions. The authors thank Eric Stewart for his guidance on the fundamentals of mechanical modeling. This research was supported by Advanced Research Projects Agency-Energy (Award No. DE-AR0001130).

Appendix A

Table A1
Material Properties for 3C-SiC (β -SiC) [39,40].

Parameter	Value	Description
E_{SiC}	345 GPa	Young's modulus, sintered
ν_{SiC}	0.18	Poisson's ratio
ρ_{SiC}	3160 kg/m ³	Density
α_{SiC}	$4.7 \times 10^{-6} \text{ K}^{-1}$	Coefficient of thermal expansion, 0–1973 K
σ_{UCS}	5000–9000 MPa	Ultimate strength in compression
σ_{UTS}	350–650 MPa	Ultimate strength in tension
K_{SiC}	2.5–4 MPa m ^{-0.5}	Fracture toughness
λ_{SiC}	40–130 W/mK	Thermal conductivity
a_{SiC}	$30\text{--}100 \times 10^{-6} \text{ m}^2/\text{s}$	Thermal diffusivity

Appendix B

Mesh refinement studies reported in this appendix were done to ensure high-precision results for each numerical model. A meshing study was conducted for the fluidic model as shown in Fig. B1(b). The inlet flow was defined with a uniform velocity and inlet temperature, and the boundary condition of the fluidic flow was set as non-slip condition.

A total of 4,778,976 elements were created in the simulation domain for the microchannel array, as shown in Fig. B2(a). The inlet flows were assigned with the inlet temperatures. In the effective medium model, the overall domain size remained the same, with the microchannels replaced by two different homogeneous media, separated by a thin SiC wall, as shown in Fig. B2(b), meshed by 159,227 elements. The effect of meshing was investigated in Fig. B2(c), indicating that Mesh 3 was sufficient for the detailed microchannel array simulation in Fig. 4(a).

Four macrochannels were constructed as the simulation domain for the overall heat exchanger core optimization. Inside

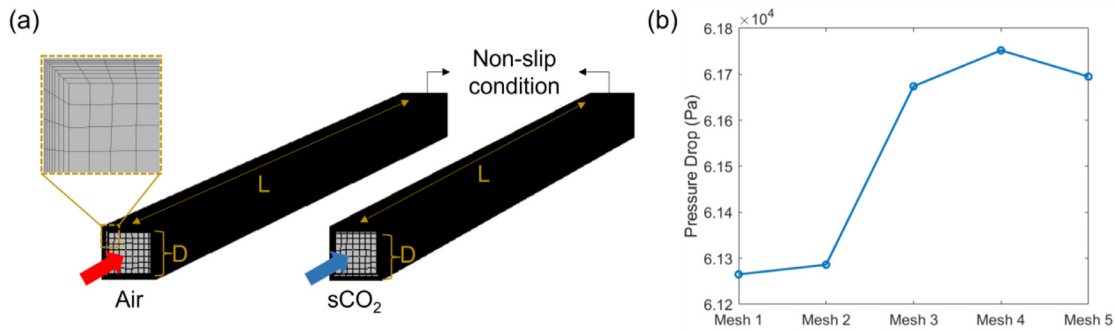


Fig. B1. Domains and meshing study for individual microchannel fluid simulations. (a) Boundary layer properties are defined as 8 layers with a stretching factor of 1.2, automatic thickness prescribed for the first layer, and a thickness adjustment factor of 5, all recommended parameters set as default for laminar flow in COMSOL [26]. (b) Mesh 1–5 represent different meshing configurations, with 98,490, 147,000, 382,200, 691,236 and 1,550,808 elements, respectively.

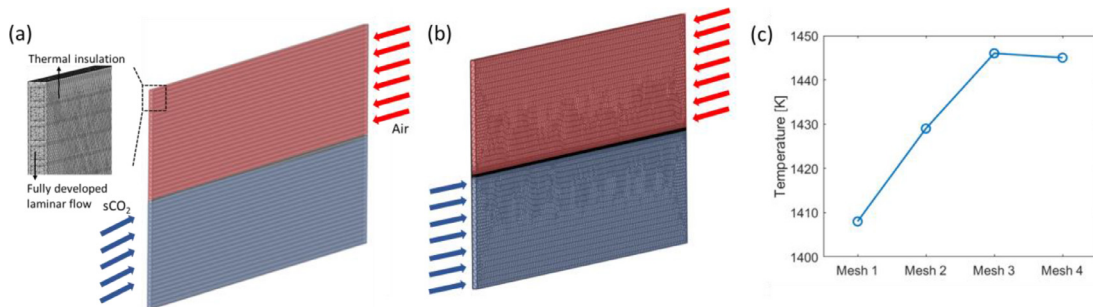


Fig. B2. Domains and meshing study for microchannel network and effective medium model. (a) 50 microchannels are included in the simulation domain to study the heat transfer in the microchannel network. Air flows through the top 25 microchannels and sCO₂ in the bottom 25 microchannels in opposite directions. The zoomed-in figure shows the meshing for the detailed microchannel array, with a total of 4,778,976 elements as small as 15 μm. (b) Homogenous media are included to replace the detailed microchannels, with 159,227 elements as small as 15 μm. (c) Mesh 1–4 represent different meshing configurations for the detailed microchannel array in (a), with 206,403, 837,688, 4,778,976 and 10,234,094 elements, respectively.

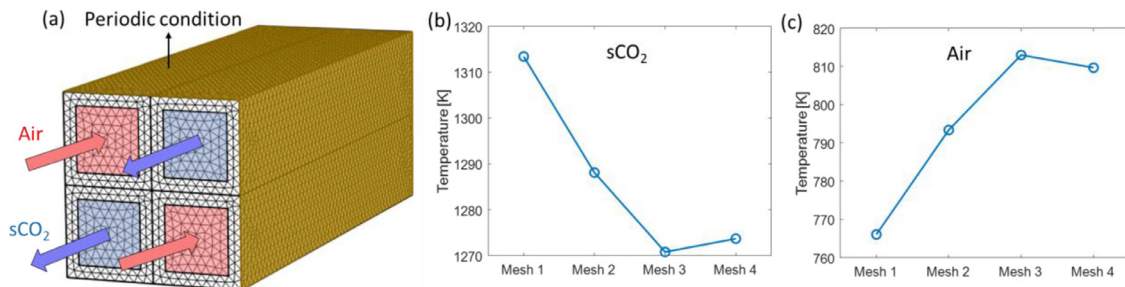


Fig. B3. Domains and meshing study for heat exchanger core simulations. (a) Four macrochannels in the simulation domain with a total of 227,804 elements are as small as 0.5 mm. Exterior sidewalls are assigned as periodic conditions. The area-average temperatures of the (b) sCO₂ and (c) air outlets are plotted with different meshing configurations 1–4, with 582,103, 1,981,829, 227,804 and 3,749,905 elements, respectively.

each macrochannel the fluid flow was modeled as the homogeneous media from the effective medium model. There are four macrochannels in the simulation domain with a total of 227,804 elements as small as 0.5 mm, as shown in Fig. B3(a). Fig. B3(b, c) demonstrates that the current meshing configuration (mesh 3) is sufficient to produce accurate results for the heat exchanger core optimization.

For the structural simulation, a triangular mesh was employed with 33,562 elements spaced variably, ranging from 1 to 0.3 mm. Refined mesh was applied at the filleted corners of each macrochannel to ensure numerical convergence. A mesh-dependent analysis in Fig. B4 shows negligible variability in the solution (< 0.001 relative error) for the current mesh size, confirming the numerical accuracy of the simulation.

Both fluid and thermal simulations use a generalized minimal residual (GMRES) iterative method with a relative tolerance con-

vergence criterion of 0.001. Structural simulations use a multi-frontal massively parallel sparse (MUMPS) direct linear solver with a relative tolerance convergence criteria of 0.001 [41].

A Grid Convergence Index (GCI) metric [42] was calculated for each mesh independence analysis, for all simulated cases, as given by

$$GCI_1 = F_s \frac{|f_2 - f_1|}{r^p - 1} = r^p \times GCI_2 \tag{B1}$$

where subscript 1 indicates the finer mesh and 2 the coarser, r is the grid ratio of fine mesh to coarse mesh, p is the order of method (set as 2 in COMSOL), f is the model solution of interest, and F_s is a factor of safety over the Richardson error estimator, prescribed by convention as 3 [42]. For Fig. B1, GCI of the reported mesh 3 dataset is 0.56%. For Fig. B2, GCI of the reported mesh 3 dataset is 0.27%. For Fig. B3, GCI of the reported mesh 3 dataset is 1.10%.

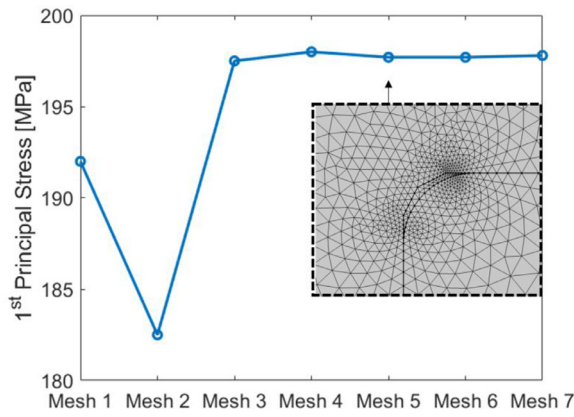


Fig. B4. Meshing study of the 1st principal stress analysis. Meshes 1–7 consist of minimum element sizes of 0.02 mm, 0.019 mm, 0.011 mm, 0.005 mm, 0.003 mm, 0.001 mm, and 0.0005 mm, respectively. Convergence of 1st principal stress magnitudes averaged along fillet is achieved with meshes 3–7, with 0.1 MPa variation between Meshes 5–7, with 0.1 MPa variation between Meshes 5–7. Mesh 5 was selected to minimize computational complexity while demonstrating high fidelity results.

For Fig. B4 GCI of the reported mesh 5 dataset is 0.02%. Thus all meshes show sufficient convergence of results.

Appendix C

For a heat exchanger design of $D = 140 \mu\text{m}$, $t_w = 60 \mu\text{m}$ microchannels, 625 microchannels per macrochannel, entrance lengths were estimated using inlet material properties for both working fluids, evaluated at the inlet temperatures, given as below

$$d_{fluid, sCO_2} \approx 0.05ReD = 10 \text{ mm}, \tag{C1}$$

$$d_{thermal, sCO_2} \approx 0.05RePrD = 8 \text{ mm}, \tag{C2}$$

$$d_{fluid, air} \approx 0.05ReD = 6 \text{ mm}, \tag{C3}$$

$$d_{thermal, air} \approx 0.05RePrD = 4 \text{ mm}. \tag{C4}$$

Based on the heat exchanger core, both fluids reach fully developed flows in the microchannels.

We approximated our fluid flows as laminar flows in a smooth square duct and estimated pressure drop ΔP_{micro} using the Darcy-Weisbach empirical equation with average flow velocity $\langle u \rangle$ [43],

Table C1
Pressure drop simulation compared to previous literature results.

	sCO ₂	Air
Model [u_{max}/u]	2.07	2.01
Reference [u_{max}/u]	2.09	2.09
Difference [%]	1	4

given by

$$\Delta P_{micro} = \frac{56.9\mu\langle u \rangle L}{2D^2}, \tag{C5}$$

$$\langle u \rangle = \dot{m}_f / D_M^2 \phi / \rho, \tag{C6}$$

where \dot{m}_f is the mass flow rates per macrochannel, ρ is fluid density. With the same hydraulic diameter and mass flow rates, the pressure drop scales with $1/\phi$.

The results of pressure drop were compared to numerical COMSOL simulations as shown in Fig. C1. The expected pressure drop maintained $< 1\%$ for thermal applications. Darcy-Weisbach empirical model assumes fully developed laminar flows while the numerical model includes the effect of entrance length. The difference slightly increases with larger channel sizes due to the longer entrance length. Overall, the Darcy-Weisbach empirical equation provides an effective and efficient approach to estimate the pressure drop based on the design space.

The fluid profile u_{max}/u was compared to well-established values by Shah and London to further ensure accuracy of our pressure drop simulations [44].

With the Darcy-Weisbach equation, we plotted the pressure drops based on the microporosity in the macrochannel cores, with the same hydraulic diameter and mass flow rates, as shown in Fig. C2. Smaller porosity increases the flow velocities and leads to higher pressure drops (Table C1).

The fluidic model as presented in the work is for initial estimation of pressure drop, which uses constant material properties based on inlet conditions for rapid optimization of the geometry. For a more accurate prediction of pressure drop in the microchannel for our optimized geometry, we present the following analysis with temperature dependent thermophysical properties. Fig. C3 shows a $D = 140 \mu\text{m}$, $t_w = 60 \mu\text{m}$ microchannel, with inlet flow conditions of $u_c = 1.34 \text{ m/s}$ and $u_h = 17.83 \text{ m/s}$ for sCO₂ and air, respectively. This corresponds to a macrochannel microporosity of 50%. Applied with expected thermal profiles, we are able to vary both air and sCO₂ material properties with respect to temperature

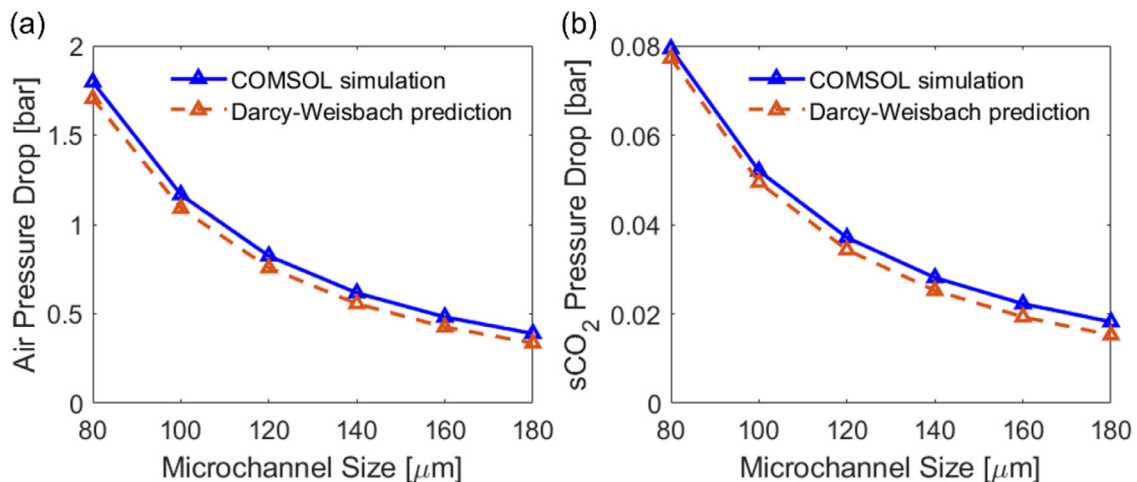


Fig. C1. Comparison between microchannel pressure drop as simulated in the numerical fluidic model (Fig. 4) and as estimated using Darcy-Weisbach equation. Both the air (left) and sCO₂ (right) microchannels show good agreement between numerical simulation and empirical approximation, with a slight increase in variation at larger microchannel sizes attributed to entrance length effects.

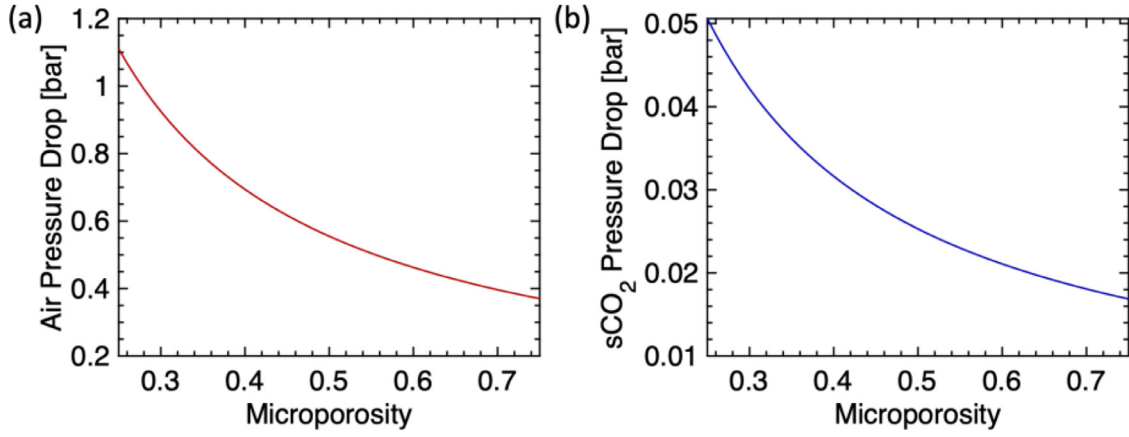


Fig. C2. The effect of microporosity on pressure drops of (a) air and (b) sCO₂ flows.

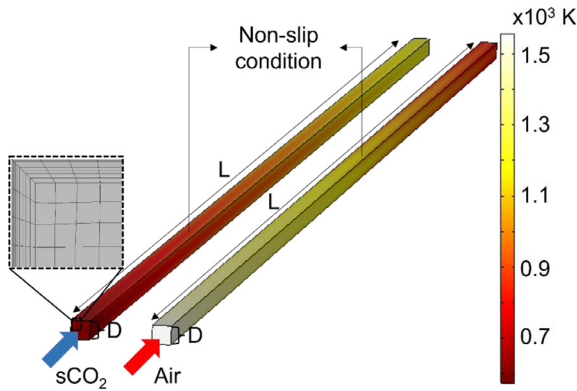


Fig. C3. Microchannel fluidic model with temperature dependent material properties. Thermal profiles are obtained from the thermal model with 50% porosity, corresponding to 625 microchannels each with a geometry of $D = 140 \mu\text{m}$, $t_w = 60 \mu\text{m}$. Heat flux per porous macrochannel is averaged by 625 microchannels to obtain the heat flux into/out of the working fluid within a single average microchannel for each fluid.

[45,46]. The results show predicted pressure drops of 3.5 kPa for sCO₂ and 53.1 kPa for air, a 0.01% and 0.7% pressure loss in each working fluid, respectively.

The effect of thermal entrance length can be estimated based on the average Nusselt numbers [47] for both fluids, given as

$$\bar{Nu} = 3.61 + \frac{0.0668 (D/L) Re_D Pr}{1 + 0.04 ((D/L) Re_D Pr)^{2/3}} = 3.74 \sim 3.82 \quad (C7)$$

which represents about 5% of thermal enhancement of the convective heat transfer with fully developed laminar flow.

Appendix D

Radiation can play a significant role in heat transfer at high temperatures. However, in our heat exchanger design, radiative effects can be neglected because it is less than 4% of the convective and conductive heat transfer. This is mainly attributed to the small microchannel size featured in our design. The operating temperature range of the air flow channels is approximately 1065 to 1558 K, while the temperature of sCO₂ channels ranges from approximately 573 to 1065 K. This indicates that for our 50% effectiveness heat exchanger core design, the temperature difference across each microchannel is approximately 20 K.

Since air is transparent to thermal radiation at this temperature range [48], thermal radiation from the higher temperature SiC microchannel wall to the opposed lower temperature SiC microchan-

nel wall contributes to the radiative heat transfer. The emissivity of SiC in the above operating condition is characterized to be 0.85 [49]. Using $t_w = 60 \mu\text{m}$ and $D = 140 \mu\text{m}$, the effective thermal conductivity of the microchannel network is

$$k_{eff} = \frac{t_w (D + t_w)}{t_w^2 + D^2 + D t_w} k_{sic} \approx 16 \text{ W/mK}. \quad (D1)$$

Therefore, the conductance, h_{cond} , through the microchannel walls is

$$h_{cond} = \frac{1}{R''_{cond}} \sim \frac{k_{eff}}{t_w} = 267 \text{ kW/m}^2\text{K}. \quad (D2)$$

On the other hand, the radiative heat transfer coefficient from the high-temperature to the low-temperature microchannel walls with a highest temperature of 1558 K is given by,

$$h_{radiation} \sim \sigma \epsilon_{sic} (T_{w1}^2 + T_{w2}^2) (T_{w1} + T_{w2}) \sim 700 \text{ W/m}^2\text{K}, \quad (D3)$$

where T_{w1} and T_{w2} represent the temperatures of the microchannel walls. This indicates that when comparing h_{cond} to $h_{radiation}$, $h_{radiation}$ only accounts for 0.3% of the overall heat transfer, which is negligible in our thermal analysis. sCO₂ is not fully transparent to thermal radiation in the operating temperature range (from 573 to 1065 K). sCO₂ acts as a participating media, with an experimentally characterized emissivity of 0.2 [50]. Prior work has indicated negligible contribution of sCO₂ as a participating media with small tube diameters below a few millimeters [51]. To further confirm the insignificant role of thermal radiation, we compared it with the convection from the SiC microchannel wall to sCO₂ in a $D = 140 \mu\text{m}$ microchannel. The convection heat transfer coefficient is given by,

$$h_{convection} = \frac{Nu k_{sCO2}}{D} \sim 2500 \text{ W/m}^2\text{K}. \quad (D4)$$

Based on an absorption coefficient of $10^4/\text{m}$ [52], radiation from the SiC microchannel wall is attenuated to about 25% across a 140 μm microchannel, indicating that 75% of the radiation is absorbed by sCO₂ working fluid. Therefore, the radiative heat transfer coefficient is estimated as

$$h_{radiation} \sim 0.75 \sigma \epsilon_{sic} (T_{sic}^2 + T_{sCO2}^2) (T_{sic} + T_{sCO2}), \quad (D5)$$

where $h_{radiation}$ ranges from 27 W/m²K to 192 W/m²K, T_{sic} and T_{sCO2} represent the solid SiC and sCO₂ temperatures. Both temperatures increase from 573 to 1558 K across the entire microchannel length. Therefore, the average radiative heat transfer coefficient throughout the entire microchannel can be calculated as follows,

$$\bar{h}_{radiation} = \frac{1}{L} \int_{T_{lo}}^{T_{hi}} h_{radiation} dx \sim 96 \text{ W/m}^2\text{K}. \quad (D6)$$

Therefore, for sCO₂, the radiative heat transfer is 3.9% of the convective heat transfer. Convection is still the dominant heat transfer mode between SiC and sCO₂ and the radiative heat transfer can be neglected in our proposed heat exchanger design.

Appendix E

The effectiveness is enhanced by the channel length or NTU as shown in Fig. E1, using the 7 mm microchannel design in Fig. 6(b). Due to the high surface area to volume ratio, the length of the heat exchanger core can be less than 15 cm for an effectiveness of 0.9 or even under 5 cm for an effectiveness of 0.7.

With a short channel length and large thermal gradient, it is essential to evaluate the heat transfer contributed by the conduction heat transfer along the channels within the solid phase materials. Here we investigated the impact of solid thermal conductivity on the heat transfer along the channels, and compared it with convective heat transfer.

A microchannel in this design has a size of $D = 140 \mu\text{m}$, wall thickness of $t_w = 60 \mu\text{m}$, length $L = 4 \text{ cm}$. SiC thermal conductivity k_{SiC} ranges from 40 to 130 W/mK. The macrochannel wall thickness is $t_M = 1 \text{ mm}$, with a porous core of $D_M = 5 \text{ mm}$. In one macrochannel, there are $N = (D_M / (D + t_w))^2 = 625$ microchannels in total.

For solid conductive heat transfer along the macrochannel, the total cross section area A_{cond} per macrochannel is given by,

$$A_{\text{cond}} = (D_M + t_M)^2 - \phi D_M^2 = 36.5 \text{ mm}^2 \quad (\text{E1})$$

where ϕ represents the microporosity of the microchannel network, which is given by,

$$\phi = \frac{D^2}{(D + t_w)^2} \sim 0.5. \quad (\text{E2})$$

We can compare the conductive resistance through solid phase along the macrochannel to the convective resistance between the working fluids to the solid walls, which can be expressed by the Biot number,

$$Bi = \frac{L/k_{\text{SiC}}/A_{\text{cond}}}{1/(h_{\text{conv}}4DLN)} \quad (\text{E3})$$

where the convective heat transfer coefficient h_{conv} is given by,

$$Nu = \frac{h_{\text{conv}}D}{k_{\text{fluid}}} = 3.61. \quad (\text{E4})$$

Substituting Eq. (E4) into Eq. (E3), we obtained,

$$Bi = \frac{4N Nu k_{\text{fluid}}L^2}{k_{\text{SiC}}A_{\text{cond}}} = \frac{k_{\text{fluid}}}{k_{\text{SiC}}} \frac{4N NuL^2}{A_{\text{cond}}} = \frac{k_{\text{fluid}}}{k_{\text{SiC}}} 633 N$$

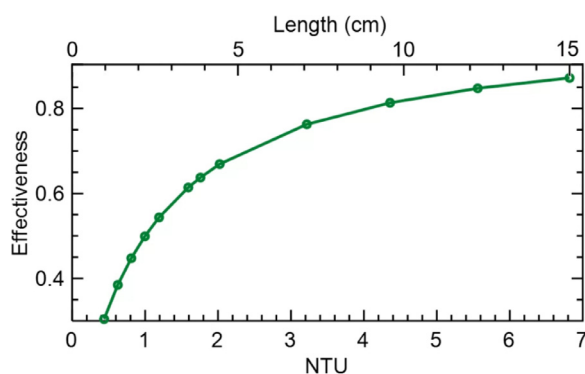


Fig. E1. The effects of NTU and channel length on the overall heat exchanger effectiveness.

$$= 3.96 \times 10^5 \frac{k_{\text{fluid}}}{k_{\text{SiC}}} \geq 150 \quad (\text{E5})$$

where k_{SiC} ranges from 40 to 130 W/mK within the operating temperatures, and k_{fluid} is 0.05–0.1 W/mK for working fluids considered in our work. Eq. (E5) indicates that the conduction contribution of the solid along the macrochannel is much smaller than convection owing to the high surface area to volume ratio and enhanced convective heat transfer coefficient enabled by the microchannel design.

Appendix F

Due to the large temperature gradient during the heat exchanger operation, we investigated the impact of thermal stress on our proposed design, which is critical to the safety operation. The heat exchanger core's response to thermal deformation depends highly on the thermal gradient and zero residual stress state temperature of the SiC, requiring an adjustment to our previous structural evaluation. Fig. F1 shows how the principal stresses vary depending on the zero residual stress state temperature. To model the stress distribution during the heat exchanger operation, the temperature distribution predicted by the thermal model was used as the input of the structural model, as shown in Fig. F1(a, b). All other boundary conditions remain the same as our analysis in Mechanical Stress Modeling. L_1 to L_4 represent various locations regarding channel length and hence different temperatures. We focused on the thermal stress perpendicular to the flow direction due to the large pressure difference and temperature gradient between the two working fluids. In Fig. F1(c), with low residual stress state temperatures, thermal gradients at low temperatures (cross sections L_1 and L_2) play a minimal role in tensile stress and therefore maximum 1st principal stress values are similar to those in the pressure loading only model (200 MPa). However, due to the low stress-free temperature, higher temperature regions (L_3 and L_4) see an increase in the 3rd principal, compressive stresses. Conversely, at high residual stress state temperatures, low temperature cross-sections see a dramatic increase in 1st principal, tensile stresses.

Based on the results of the structural modeling, thermal stresses have negligible impact on the tensile stresses generated in the heat exchanger core given the SiC material is stress-free at temperatures below 700 K after fabrication, which is achievable by slow cooling cycles after sintering completion.

Appendix G

The coextrusion process has shown promise in producing consistent microchannels with various materials for microchannels as small as 50 μm [27]. The choice of microchannels around 100 μm suits the pressure drop requirement and is also reasonable based on the current development of the ceramic co-extrusion process. Nevertheless, there could be fabrication defects regarding microchannels, such as surface roughness, blockage, merging channels, and distorted microchannels.

Due to the grain size and possible fabrication defects, surface roughness ($\sim \mu\text{m}$) can be expected on the microchannel walls. Because of the laminar flow in the microchannels, the overall surface roughness has negligible effect on the pressure drop or thermal performance.

Blocked microchannels will reduce the surface area and also increase the pressure drop. Each 1% blockage of the microchannel will reduce the surface area by about 1%. Since the heat transfer conductance across the solid phase is not affected, the overall thermal performance reduction will be less than 1%. Pressure drop will increase on the scale of 1% due to higher flow velocity in other mi-

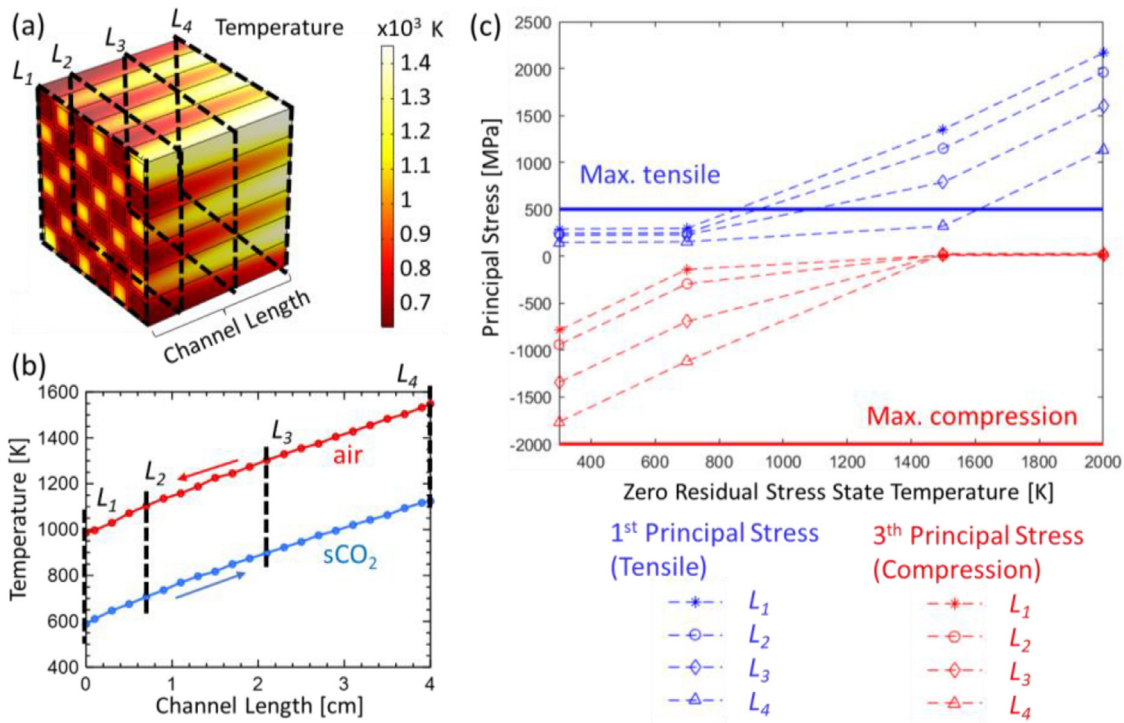


Fig. F1. Thermal structural model of heat exchanger core. (a) Thermal gradients in an example 6×6 heat exchanger core. The dashed lines represent the cross sections at different channel length locations. (b) Temperatures of the heat exchanger core at varying lengths (L_1 to L_4), where temperature data was extracted and used as an input for the 2D structural modeling. (c) Maximum 1st (blue) and 3rd (red) principal stress results of the 2D structural modeling, including both thermal gradient and pressure loading conditions, for each of the cross sections along the channel length.



Fig. G1. Schematic of perfect square microchannels (left) and slanted rhombus microchannels with an angle of θ .

crochannels, as the pressure drop scales linearly with velocity for laminar flow.

Assuming the original microchannel size is $D_{h,1} = D$, two adjacent microchannels merging together reduces the surface area from $8D$ to $6D$, a reduction of 0.25% for each 1% of merging microchannels. The hydraulic diameter of the two adjacent merged microchannels becomes $D_{h,2} = \frac{4A_c}{P} = \frac{4}{2+1}D = \frac{4}{3}D$. Therefore, it reduces the pressure drop to $(\frac{3}{4})^4$, leading to about 3% pressure drop for each 1% of merging microchannels.

Another possible defects can lead to rhombus-shaped microchannels rather than square-shaped microchannels during the co-extrusion process. With a slanted angle of θ as shown in the Fig. G1, the overall cross section area of the microchannel remains the same, but with a higher surface area $A_\theta/A = (1 + 1/\sin(\theta))/2$ and smaller hydraulic diameter $D_\theta/D = 2/(1 + 1/\sin(\theta))$. For example, even with an average slanted angle of 70° , the surface area is enhanced by about 3.2% with a higher pressure drop by 3.1%.

Overall, these defects have minor effects on heat transfer and pressure drop with low defect rates, which is reasonable based on the established co-extrusion process [27].

Since the overall microporosity within the macrochannel remains similar or lower when the microchannels are filled or

blocked, the mechanical strength will stay the same value or slightly increase, maintaining a similar safety factor.

Appendix H

The hierarchical model mainly focuses on the heat exchanger core and does not include the pressure drop from the headers. A possible header design for checkerboard-pattern counterflow heat exchangers [53] is illustrated in Fig. H1(a). By offsetting a part of the macrochannels from even and odd columns half of the macrochannel size, a checkerboard pattern is rearranged into a plate type pattern, aligning both hot and cold channels horizontally, as shown in Fig. H1(b). This can then be interfaced with standard linear or plate-type headers to attach the heat exchanger to the rest of the cycle. The header can be made from macrochannels and integrated with the core to assist the fluidic distribution to the respective macrochannels with minimal pressure drop and flow maldistribution. In the future work, it is important to optimize and implement the header design, and characterize the pressure drop as well.

Appendix I

The proposed heat exchanger can further be customized for other applications including terrestrial power generation plants, such as nuclear power plants and concentrated solar power systems. Here we included an example for a concentrated solar power system, where the working fluids are molten salt at 873 K, 72.5 kg/s and sCO_2 at 1073 K, 80 kg/s [14]. Compared to existing solar applications, the elevated temperatures will continue enhancing energy conversion efficiency and lowering the levelized cost of electricity [54]. To compensate for the higher viscosity of the molten salt, we adopted an asymmetrical design for two working fluids, assigning millimeter-scale channels (0.7 mm microchannel

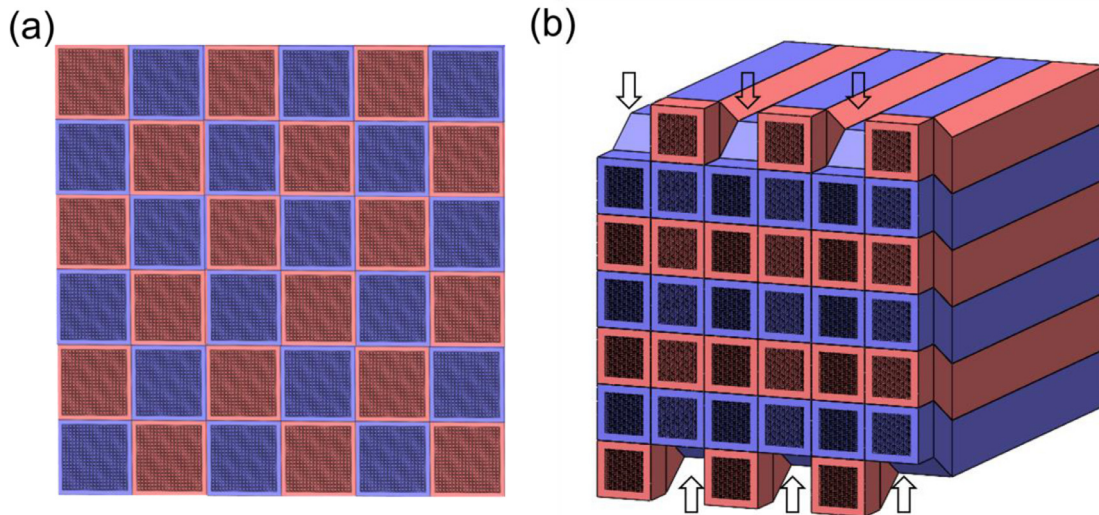


Fig. H1. Schematic header design for the checkerboard counterflow heat exchanger. (a) Schematic of the checkerboard macrochannels of the heat exchanger core. Red and blue cells represent macrochannel for hot and cold flows. (b) Through offsetting the start and the end of macrochannels in odd columns downwards by half unit cell size, and even columns up by half unit size, the cold and hot macrochannels align horizontally at inlets and outlets to assist the distribution of working fluids with respective macrochannels.

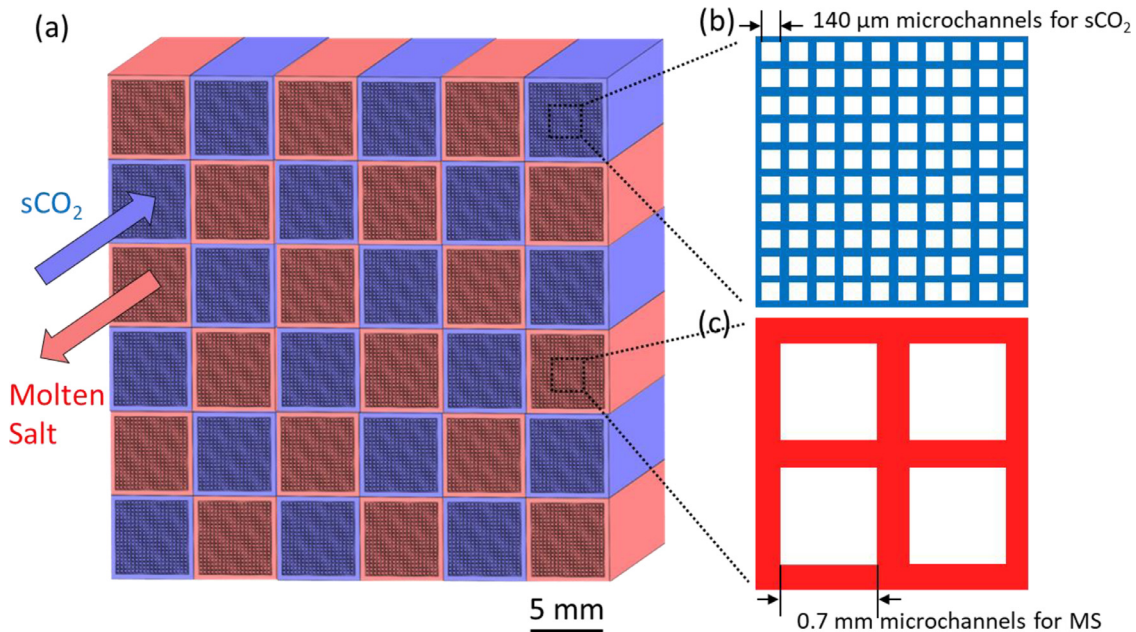


Fig. 11. Multiscale porous heat exchanger core design for concentrated solar power generation, with an asymmetrical design for two working fluids. (a) Macrochannel dimensions remain identical for sCO_2 and molten salt (MS) fluids. To compensate for the higher viscosity of the molten salt, an asymmetrical design was adopted to, assign microchannels (b) for sCO_2 (140 μm microchannel and 60 μm microchannel wall) and millimeter-scale (c) channels (0.7 mm microchannel and 0.3 mm microchannel wall) for molten salt.

and 0.3 mm microchannel wall) for molten salt with smaller microchannels for sCO_2 (140 μm microchannel and 60 μm microchannel wall), illustrated by Fig. 11. The macrochannel size and wall thickness for each fluid are kept the same. Our proposed heat exchanger design can achieve a thermal duty of 17.5 MW_{th}, 95% effectiveness, power densities of 9.71 MW/m³ and 4.05 kW/kg, more than 2.5× thermal performance compared to printed-circuit heat exchangers with similar materials [2,11,14].

References

[1] A. Henry, R. Prasher, A. Majumdar, Five thermal energy grand challenges for decarbonization, *Nat. Energy* 59 (5) (2020) 635–637 2020.

[2] Scott R. Penfield, Compact Heat Exchangers for Nuclear Power Plants. https://energy.mit.edu/wp-content/uploads/2017/02/2-1-Penfield_Compact-Heat-Exchangers-for-NPPs-170130-min.pdf (accessed May 6, 2022)

[3] R. Brun, K. Friedman, P. Dennis, Fundamentals and Applications of Supercritical Carbon Dioxide (sCO_2) Based Power Cycles, Woodhead Publishing, 2017.

[4] C. Behar, Technology Roadmap Update for Generation IV Nuclear Energy Systems, in: OECD, Nucl. Energy Agency Gener. IV Int. Forum, Vol. 17, No. 2018, 2014, pp. 19–52.

[5] Very-High-Temperature Reactor (VHTR), https://www.gen-4.org/gif/jcms/c_42153/very-high-temperature-reactor-vhtr (accessed March 3, 2022).

[6] Molten Salt Reactor (MSR), https://www.gen-4.org/gif/jcms/c_9359/msr (accessed May 5, 2022).

[7] H.E., Rohlik, 1983, August. Current and future technology in radial and axial gas turbines. In *Seminar on Fluid Dyn. of Turbomachinery* (No. E-1702).

[8] General Electric Company, The Art Of Engineering: The World’s Largest Jet Engine Shows Off Composite Curves, *GE reports*, April 28, 2016.

- [9] GE Aviation, GE90 Engine family, <https://www.geaviation.com/propulsion/commercial/ge90> (accessed May 5, 2022).
- [10] X. Zhang, H. Keramati, M. Arie, F. Singer, R. Tiwari, A. Shooshtari, M. Ohadi, Recent developments in high temperature heat exchangers: a review, *Front. Heat Mass Transf.* 11 (2018) 1–14.
- [11] L. Chordia, M.A. Portnoff, E. Green, High temperature heat exchanger design and fabrication for systems with large pressure differentials, No. DE-FE0024012, Pittsburgh, PA (United States), 2017.
- [12] S.A. David, J.A. Siefert, J.N. DuPont, J.P. Shingledecker, Weldability and weld performance of candidate nickel base superalloys for advanced ultrasupercritical fossil power plants part I: fundamentals, *Sci. Technol. Weld. Join.* 20 (2015) 532–552.
- [13] Kenneth Henry Sandhage, Methods for manufacturing ceramic and ceramic composite components and components made thereby, US20190381600A1, 2017.
- [14] M. Caccia, M. Tabandeh-Khorshid, G. Itkos, A.R. Strayer, A.S. Caldwell, S. Pidaparti, S. Singnisai, A.D. Rohskopf, A.M. Schroeder, D. Jarrahbashi, T. Kang, S. Sahoo, N.R. Kadasala, A. Marquez-Rossy, M.H. Anderson, E. Lara-Curzio, D. Ranjan, A. Henry, K.H. Sandhage, Ceramic–metal composites for heat exchangers in concentrated solar power plants, *Nature* 562 (2018) 406–409.
- [15] M.A. Arie, A.H. Shooshtari, V.V. Rao, S.V. Dessiatoun, M.M. Ohadi, Air-side heat transfer enhancement utilizing design optimization and an additive manufacturing technique, *J. Heat Transf.* 139 (3) (2017) 1–12 031901.
- [16] M.A. Arie, A.H. Shooshtari, M.M. Ohadi, Experimental characterization of an additively manufactured heat exchanger for dry cooling of power plants, *Appl. Therm. Eng.* 129 (2018) 187–198.
- [17] M. Ohadi, K. Choo, S. Dessiatoun, E. Cetegen, Next Generation Microchannel Heat Exchangers, Springer Verlag, 2013.
- [18] X. Zhang, R. Tiwari, A.H. Shooshtari, M.M. Ohadi, An additively manufactured metallic manifold-microchannel heat exchanger for high temperature applications, *Appl. Therm. Eng.* 143 (2018) 899–908.
- [19] W.D. Gerstler, D. Erno, Introduction of an additively manufactured multi-furcating heat exchanger, in: Proceedings of the 16th Intersociety Conference on Thermal and Thermomechanical Phenomena in Electronic Systems (ITHERM), 2017, pp. 624–633. 2017.
- [20] Metal additive manufacturing enables lean, green heat exchanger, <https://www.makepartsfast.com/metal-additive-manufacturing-enables-lean-green-heat-exchanger/> (accessed March 3, 2022).
- [21] S.K. Mylavarapu, X. Sun, R.N. Christensen, R.R. Unocic, R.E. Glosup, M.W. Patterson, Fabrication and design aspects of high-temperature compact diffusion bonded heat exchangers, *Nucl. Eng. Des.* 249 (2012) 49–56.
- [22] W.Q. Wang, Y. Qiu, Y.L. He, H.Y. Shi, Experimental study on the heat transfer performance of a molten-salt printed circuit heat exchanger with airfoil fins for concentrating solar power, *Int. J. Heat Mass Transf.* 135 (2019) 837–846.
- [23] R. Cavalcanti Alvarez, A.P.C. Sarmiento, L.H.R. Cisterna, F.H. Milanese, M.B.H. Mantelli, Heat transfer investigation of a 90° zigzag channel diffusion-bonded heat exchanger, *Appl. Therm. Eng.* 190 (2021) 116823.
- [24] A.P.C. Sarmiento, V.H.T. Soares, G.G. Carqueja, J.V.C. Batista, F.H. Milanese, M.B.H. Mantelli, Thermal performance of diffusion-bonded compact heat exchangers, *Int. J. Therm. Sci.* 153 (2020) 106384.
- [25] K.K. Chawla, *Composite Materials: Science and Engineering*, 3rd ed., Springer, 2012 third edition.
- [26] C. Van Hoy, A. Barda, M. Griffith, J.W. Halloran, Microfabrication of ceramics by co-extrusion, *J. Am. Ceram. Soc.* 81 (2005) 152–158.
- [27] A.T. Crumm, J.W. Halloran, Fabrication of microconfigured multicomponent ceramics, *J. Am. Ceram. Soc.* 81 (1998) 1053–1057.
- [28] T. Garbacz, J.W. Sikora, Co-extrusion process, *J. Am. Ceram. Soc.* 1 (2010) 2008–2011.
- [29] COMSOL, Boundary layer properties, https://doc.comsol.com/5.5/doc/com.comsol.help.comsol/comsol_ref_mesh.15.25.html (accessed March 3, 2022).
- [30] F. Beer, E. Johnston, J. DeWolf, D. Mazurek, *Mechanics of Materials*, 5th ed., McGraw-Hill, 1999 5th Editio.
- [31] W. Pabst, E. Gregorová, G. Tichá, Elasticity of porous ceramics - a critical study of modulus-porosity relations, *J. Eur. Ceram. Soc.* 26 (2006) 1085–1097.
- [32] L. Anand, S. Govindjee, *Continuum Mechanics of Solids*, Oxford University Press, 2020.
- [33] COMSOL Multiphysics, Structural Mechanics Module User's Guide version 5.3, (2018) 454, <https://doc.comsol.com/5.3/doc/com.comsol.help.sme/StructuralMechanicsModuleUsersGuide.pdf> (accessed May 5, 2022).
- [34] Y.W. Kim, M. Mitomo, H. Hirotsuru, Grain growth and fracture toughness of fine-grained silicon carbide ceramics, *J. Am. Ceram. Soc.* 78 (1995) 3145–3148.
- [35] EXXENTIS, Porous aluminum foam, <https://www.exxentis.co.uk/> (accessed May 5, 2022).
- [36] R.K. Shah, D.R. Sekulib, *Heat Exchangers*, McGraw-Hill, New York, 1998.
- [37] Q. Li, G. Flamant, X. Yuan, P. Neveu, L. Luo, Compact heat exchangers: a review and future applications for a new generation of high temperature solar receivers, *Renew. Sustain. Energy Rev.* 15 (2011) 4855–4875.
- [38] Characteristics of diffusion-bonded heat exchangers, <https://www.heatric.com/heat-exchangers/features/characteristics/> (accessed March 3, 2022).
- [39] T. Ohji, *Handbook of Advanced Ceramics - Materials, Applications, Processing, and Properties*, Academic Press, 2013.
- [40] J. Shackelford, Y. Han, S. Kim, S. Kwon, *CRC Materials Science and Engineering Handbook*, 4th edition, CRC Press, 2016.
- [41] MUMPS: a parallel sparse direct solver, <http://mumps.enseiht.fr/> (accessed March 3, 2022).
- [42] P.J. Roache, *Verification and Validation in Computational Science and Engineering*, Hermosa, 1998.
- [43] H.J. Leutheusser, Velocity distribution and skin friction resistance in rectangular ducts, *J. Wind Eng. Ind. Aerodyn.* 16 (1984) 315–327.
- [44] Y.S. Muzychka, M.M. Yovanovich, Laminar forced convection heat transfer in the combined entry region of non-circular ducts, *J. Heat Transf.* 126 (2004) 54–61.
- [45] P. J. Linstrom, NIST standard reference database number 69, NIST Chemistry WebBook (2003).
- [46] The engineering toolbox, <https://www.engineeringtoolbox.com/> (accessed March 3, 2022).
- [47] A. Mills, *Heat Transfer*, CRC Press, 1992.
- [48] Radiation transmitted by the atmosphere, <https://ei.lehigh.edu/learners/cc/greenhouse/radiationChart.png> (accessed March 3, 2022).
- [49] M. Balat-Pichelin, A. Bousquet, Total hemispherical emissivity of sintered SiC up to 1850 K in high vacuum and in air at different pressures, *J. Eur. Ceram. Soc.* 38 (2018) 3447–3456.
- [50] S.D. Khivisara, A design concept of a volumetric solar receiver for supercritical CO₂ Brayton cycle, 2018, <https://etd.iisc.ac.in/handle/2005/2996> (accessed March 3, 2022).
- [51] S.D. Khivisara, V. Srinivasan, P. Dutta, Radiative heating of supercritical carbon dioxide flowing through tubes, *Appl. Therm. Eng.* 109 (2016) 871–877.
- [52] A. Khadse, A. Curbelo, J.S. Kapat, Numerical study of radiation heat transfer for a supercritical CO₂ turbine linear cascade, in: Proceedings of the ASME Turbo Expo, American Society of Mechanical Engineers Digital Collection, 2019.
- [53] J.F. Plourde, T. Mosidis, B. Fichera, Heat exchanger with headering system and method for manufacturing same, U.S. Patent Application No.13/442,531, 2013, <https://www.patentsencyclopedia.com/app/20130264031> (accessed March 3, 2022).
- [54] M. Mehos, C. Turchi, J. Vidal, M. Wagner, Z. Ma, C. Ho, W. Kolb, C. Andracka, A. Kruienza, Concentrating solar power Gen3 demonstration roadmap, No. NREL/TP-5500-67464, National Renewable Energy Lab.(NREL), Golden, CO (United States), 2017.